Multiple phase screen modeling of ionospheric scintillation along radio occultation raypaths

Charles S. Carrano,[1] Keith M. Groves,[2] Ronald G. Caton,[3] Charles L. Rino,[4] and Paul R. Straus[5]

[1]   We present the Radio Occultation Scintillation Simulator (ROSS), which uses the multiple phase screen method (MPS) to simulate the forward scatter of radio waves by irregularities in the equatorial ionosphere during radio occultation experiments. ROSS simulates propagation through equatorial plasma bubbles which are modeled as homogeneous electron density fluctuations modulated by a Chapman profile in altitude and a Gaussian window in the magnetic east-west direction. We adjust the parameters of the density model using electron density profiles derived from the ALTAIR incoherent scatter radar (9.4°N, 167.5°E, 4.3° north dip), and space-to-ground observations of scintillation using VHF and GPS receivers that are colocated with the radar. We compare the simulated occultation scintillation to observations of scintillation from the CORISS instrument onboard the C/NOFS satellite during a radio occultation occurring near ALTAIR on 21 April 2009. The ratio of MPS predicted S_4 to CORISS observed S_4 throughout the F region altitudes of 240–350 km ranged between 0.86 and 1.14.

Citation: Carrano, C. S., K. M. Groves, R. G. Caton, C. L. Rino, and P. R. Straus (2011), Multiple phase screen modeling of ionospheric scintillation along radio occultation raypaths, *Radio Sci.*, *46*, RS0D07, doi:10.1029/2010RS004591.

1.   Introduction

[2]   Plasma instability processes operating in the equatorial ionosphere after sunset can generate large-scale depletions in the ambient electron density, called equatorial plasma bubbles, which are accompanied by intense random density variations occurring over a broad range of spatial scales (plasma turbulence). When radio waves traverse these variations, they experience random scattering and fluctuations in signal phase. These phase fluctuations result in mutual interference (diffraction) as the wave propagates, causing random fluctuations in both signal amplitude and phase referred to as scintillations. The scintillation of satellite signals can severely degrade the performance of global communications systems such as Air Force Satellite Communications (AFSATCOM) and navigation systems such as the Global Positioning System (GPS). The plasma turbulence associated with equatorial plasma bubbles is generally the most intense encountered worldwide, and the occurrence morphology depends on season, longitude, solar cycle, magnetic activity, and exhibits a high degree of night-to-night variability [*Aarons*, 1982].

Equatorial plasma bubbles constitute one of the most important space weather threats to technological systems which rely on transionospheric radio propagation.

[3]   Instruments onboard several low Earth orbiting satellites have routinely collected radio occultation observations using signals transmitted by the GPS constellation of satellites (e.g., C/NOFS, COSMIC, CHAMP, SAC-C, and PICOSat4), providing a rich source of information about the global occurrence morphology of ionospheric scintillation [e.g., *Anderson and Straus*, 2005; *Straus et al.*, 2003; *Ruggiero et al.*, 2009]. Radio occultation monitoring of scintillation is advantageous in that it can be performed on a global basis more readily than using ground-based monitoring techniques. Even worldwide networks of ground-based ionospheric monitoring instruments such as SCINDA [*Groves et al.*, 1997; *Basu et al.*, 2002; *Carrano and Groves*, 2006] provide relatively sparse coverage over the oceans.

[4]   Despite the advantage of global coverage, the long propagation path of a radio occultation signal through the ionosphere makes it difficult to determine the geographic location and spatial extent of the ionospheric irregularities responsible for the scintillation. Moreover, it is not obvious from the radio occultation signal itself what specific configuration of the plasma (e.g., a single bubble, multiple bubbles, etc.) has modulated the signal. To address these concerns, we have developed the Radio Occultation Scintillation Simulator (ROSS) which uses the multiple phase screen (MPS) method to simulate the forward scatter of radio occultation signals by irregularities in the equatorial ionosphere. For the sake of clarity, we note that our application differs from traditional occultation investigations which are aimed at measuring the

[1]Institute for Scientific Research, Boston College, Chestnut Hill, Massachusetts, USA.

[2]Air Force Research Laboratory, Space Vehicles Directorate, Hanscom AFB, Massachusetts, USA.

[3]Air Force Research Laboratory, Space Vehicles Directorate, Kirtland AFB, New Mexico, USA.

[4]Rino Consulting, Menlo Park, California, USA.

[5]The Aerospace Corp., El Segundo, California, USA.

mean refractive index profile. In this work, we specify the refractive index and evaluate its influence on the radio occultation signal. The MPS method can accommodate both small-scale structure which causes scintillation and large-scale variations which cause refraction. The ROSS model is designed to simulate radio propagation through known plasma configurations with the ultimate goal of better understanding the inverse problem, i.e., how to extract detailed information about the structure and distribution of irregularities along the propagation path from radio occultation measurements of scintillation. The use of ROSS for this purpose will be the subject of a future paper. Here, we describe the algorithm and validate it using observations from the CORISS instrument onboard the C/NOFS satellite.

[5] The ROSS algorithm constructs an inhomogeneous random field of electron density fluctuations consisting of a Chapman layer background with embedded plasma bubbles, represented as regions where the fluctuation strength has Gaussian variation in the magnetic east-west direction. A plane wave is propagated through the random field along the radio occultation path using the MPS method to obtain the signal at the receiver. We adjust the parameters of the density model using vertical electron density profiles derived from the ALTAIR incoherent scatter radar (9.4°N, 167.5°E, 4.3° north dip), and space-to-ground observations of scintillation using VHF and GPS receivers that are colocated with the radar. Finally, we compare the MPS simulated occultation scintillation to observations of scintillation from the CORISS instrument onboard the C/NOFS satellite during a radio occultation occurring near ALTAIR.

[6] The outline of this paper is as follows. In section 2 we describe the MPS technique for simulating wave propagation through inhomogeneous random media. Section 3 describes the model used to construct random fields of electron density fluctuations including plasma bubbles. Section 4 describes the specific radio occultation observation from CORISS that we will simulate in this paper. Section 5 presents observations from the ALTAIR incoherent scatter radar from which we derive the background electron density and estimate the vertical thickness of the scattering layer. Section 6 describes the VHF and GPS ground-based observations from the SCINDA network which are used to infer the zonal drift and turbulent intensity within the plasma bubble. Section 7 compares the results of our MPS simulation with observations of occultation scintillation from CORISS. Section 8 discusses the significance of these results and their applicability, and section 9 concludes the paper. Appendix A describes the technique used to infer the RMS density fluctuations from the scintillation observations.

2. The Multiple Phase Screen Method

[7] The multiple phase screen method is an efficient numerical technique for simulating the propagation of radio waves through extended random media which allows both amplitude and phase fluctuations to accumulate within the medium [Knepp, 1983; Grimault, 1998, Béniguel, 2002; Costa and Basu, 2002]. This capability is important when modeling radio occultation experiments through the ionosphere because the propagation path inside the random medium can be very long. Depending on the specific form of the propagator used, the MPS approach can provide an approximate solution to the scalar wave equation under either the parabolic approximation [Knepp, 1983] or the more general forward propagation approximation which accommodates wide-angle scatter [Rino, 2011, chapter 2]. In this paper we use the forward propagation approximation, but either approach can accommodate the modest scattering angles considered here. The MPS approach captures both small-scale structure which can lead to scintillation and the large-scale variations which cause refraction (the latter of which are the focus of traditional occultation experiments). The MPS approach has been applied to radio occultation experiments in the troposphere [Karayel and Hinson, 1997; Sokolovskiy, 2001]. The authors are not aware of previous applications of the MPS technique to occultation experiments in the ionosphere, although the closely related technique of radio wave back propagation was used by Sokolovskiy et al. [2002] to approximately locate the irregularity regions causing scintillation using GPS/MET observations.

[8] Due to the increased mobility of electrons along magnetic field lines, ionospheric irregularities tend to be highly elongated along the Earth's magnetic field. In this paper, we consider radio occultations occurring in the vicinity of the ALTAIR radar (9.4°N, 167.5°E, 4.3° north dip). Due to its close proximity to the dip equator, we can reasonably assume that (1) magnetic field lines are approximately horizontal, (2) there is negligible variation in the electron density in the magnetic north-south direction, (3) a two-dimensional propagation model in the plane perpendicular to the magnetic field is sufficient to describe the pertinent scattering phenomena, and (4) the electron density fluctuations in this plane are approximately isotropic. The geometry used for our MPS calculations is shown in Figure 1. The coordinate system is such that the y axis is directed along the magnetic field direction (toward magnetic south), the z axis is tangent to the Earth surface, and the x axis completes the right-handed orthogonal coordinate system. In our 2-D formulation there is no variation along the y direction, a consequence of which is that the Earth is effectively considered cylindrical, but changes over such large geospatial scales have negligible effect on the very much smaller radio wavelengths involved. We consider radio occultations between a GPS satellite and a receiver onboard a low Earth orbiting (LEO) satellite such as the CORISS instrument onboard C/NOFS [de La Beaujardière et al., 2004]. Because the distance between the transmitter and the scattering region is much greater than the distance between the scattering region and the receiver, it is appropriate to treat the GPS signal as a plane wave entering at the left-hand side of Figure 1. Because the orbital radius of a GPS satellite is much larger than that of a LEO satellite, we can assume the transmitter is fixed during the brief duration of an occultation (a few minutes), while the LEO satellite is in motion and samples the signal along the observation plane. The MPS simulation proceeds as follows. The simulation plane (x-z) is broken into a series of vertical layers which are replaced by thin phase screens (shown schematically as vertical lines in Figure 1) separated by vacuum. The phase change imparted by each screen is equal to the geometric optics phase delay due to propagation through that layer [Karayel and Hinson, 1997]. The boundary conditions are given in terms of a plane wave entering the domain with unit complex
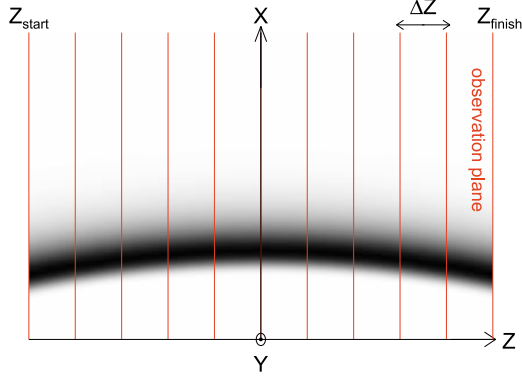
Figure 1. Geometry of the multiple phase screen calculation in the magnetic equatorial plane. The y axis is directed toward geomagnetic south, the z axis is tangent to the Earth, and the x axis completes the orthogonal system. The shaded region represents the ambient ionosphere, and the vertical lines represent phase screens which are traversed by the simulated occultation signal. The moving receiver samples the signal along the observation plane.

amplitude, e.g., $U(x, z_{start}^-) = 1$. The phase change imparted to the wave in passing through the nth screen is given by

$$U\left(x, z_n^+\right) = U\left(x, z_n^-\right) \exp\left[i \int_{z_n}^{z_{n+1}} \lambda r_e N(x, \xi) d\xi\right], \quad (1)$$

where λ is the wavelength (0.19 m in the case of the GPS L1 carrier signal), r_e is the classical electron radius, and N represents the local electron density (background plus fluctuations). Next, the wave is propagated in free space from the nth screen to the $n + 1$th screen as follows. First, the transverse Fourier transform of the complex amplitude in the x direction at the nth screen is computed according to

$$\hat{U}\left(k_x, z_n^+\right) = \int_{-\infty}^{\infty} U\left(x, z_n^+\right) e^{-ik_x x} dx, \quad (2)$$

where k_x is the wave number in the x direction. Next the Fourier components of the complex amplitude are multiplied by the so-called free-space propagator to obtain the Fourier components of the field just prior to the $n + 1$th screen:

$$\hat{U}\left(k_x, z_{n+1}^-\right) = \hat{U}\left(k_x, z_n^+\right) \exp\left[i\left(k^2 - k_x^2\right)^{1/2} \Delta z\right], \quad (3)$$

where Δz is the distance between adjacent screens. The complex amplitude of the wave just prior to the $n + 1$th screen is obtained by inverse Fourier transform:

$$U\left(x, z_{n+1}^-\right) = \frac{1}{2\pi} \int_{-\infty}^{\infty} \hat{U}\left(k_x, z_{n+1}^-\right) e^{ik_x x} dx. \quad (4)$$

These steps (equations (1) to (4)) are repeated until the observation plane ($z = z_{finish}$) is reached. This technique for propagating the wave between screens is equivalent to resolving the complex amplitude into an angular spectrum of plane waves which, due to their varying angles of propagation, travel different distances to their destination and hence arrive with different phases [Booker et al., 1950; Goodman, 2005, section 3.10]. This is the process by which diffraction occurs

and amplitude fluctuations develop. In this paper we also consider the space-to-ground propagation problem. The above algorithm can be applied in this case by interchanging the roles of x and z in equations (1)–(4).

3. Constructing Random Electron Density Fields

[9] We use a relatively simple model for equatorial plasma bubbles which are constructed as homogeneous random fluctuations characterized by an outer scale and single slope power law, and modulated by two slowly varying functions: a Chapman profile in the radial direction and a Gaussian window in the magnetic east-west direction. We begin by constructing an isotropic random field of electron density fluctuations in the plane perpendicular to the magnetic field with the following two-dimensional spatial spectrum:

$$\Phi_{\Delta N}(k_x, k_z) = 4\pi k_0^{2\nu-2} \frac{\Gamma(\nu)}{\Gamma(\nu - 1)} \frac{1}{\left(k_0^2 + k_x^2 + k_z^2\right)^\nu}. \quad (5)$$

In (5), k_x, k_z are the wave numbers in the x and z directions, respectively, $k_0 = 2\pi/L_0$ is the outer scale wave number, L_0 is the outer scale, and Γ is Euler's gamma function. The spectral slope, ν, is defined such that $p = 2\nu$ is the phase spectral index and $p^{(3)} = 2\nu + 1$ is the spectral slope of three-dimensional in situ density fluctuations. We generate a normalized 2-D random realization of electron density fluctuations with unit variance, ΔN_n, such that the ensemble average of many such realizations has the spectrum (5) throughout the domain. This is accomplished by filtering a sequence of uncorrelated Gaussian random variables as described by Knepp [1983] and also Rino [2011]. Next, we model the background electron density using a Chapman profile,

$$N_B(x, z) = NmF2 \exp\left[\frac{1}{2}\left(1 - z_c - e^{-z_c}\right)\right], \quad (6)$$

where $NmF2$ is the peak electron density and $z_c = (h - hmF2)/H$. Here, $hmF2$ is the altitude of peak electron density and H is the scale height for the electron density. In terms of our chosen coordinates, the altitude is given by $h = [(R_e + x)^2 + z^2]^{1/2} - R_e$, where R_e is the mean Earth radius. Next, we assume that the RMS of $\Delta N/N$ variations, $\sigma_{\Delta N/N}$, is independent of altitude:

$$\frac{\sigma_{\Delta N}(x, z)}{N_B(x, z)} = \sigma_{\Delta N/N} = \text{const} \quad (7)$$

In Appendix A we explain how $\sigma_{\Delta N/N}$ may be estimated from space-to-ground scintillation measurements. Note that while the background electron density contributes little to the actual scattering (in comparison with the small-scale fluctuations), in this model N_B is important because it scales the strength of the irregularities throughout the domain.

[10] Once we have generated a realization of the random field, we embed a synthetic plasma bubble by modulating the random field by a Gaussian function of Earth-centered angle:

$$B(x, z) = \exp\left\{-\left[\alpha(x, z) - \alpha_0\right]^2 / \left(2\sigma_\alpha^2\right)\right\} \quad (8)$$

where $\alpha(x, z) = \tan^{-1}[z/(x + R_e)]$ is the Earth-centered angle and α_0 is the Earth-centered angle at which a Gaussian

plasma bubble is to be introduced. This angle is related to the horizontal coordinate of the bubble, z_0, according to $\alpha_0 = \tan^{-1}[z_0/(hmF2 + R_e)]$. We specify the standard deviation of the Gaussian bubble, σ_α, in terms of the horizontal (east-west) extent of the bubble, L_H, according to $\sigma_\alpha = L_H/[A(hmF2 + R_e)]$. Here A is a scaling factor that relates the width of the Gaussian to its standard deviation. There are several reasonable ways to specify A, including the full width at half maximum (FWHM) convention which gives $A = 2(2\ln2)^{1/2} \approx 2.355$, and the full width that includes half the area (FWHA) convention which gives $A = 2(2^{1/2})\text{erf}^{-1}(1/2) \approx 1.348$. We obtained slightly better results using the FWHA convention in our simulations. Finally, we add the density fluctuations to the background density to obtain the total density field for use in our MPS simulations:

$$N(x,z) = N_B(x,z)\left[1 + \Delta N_n(x,z)\sigma_{\Delta N/N}B(x,z)\right] \qquad (9)$$

We can introduce multiple plasma bubbles by a straightforward extension of (9). The inhomogeneous random field constructed in this fashion has a local RMS $\Delta N/N$ which is independent of altitude but varies as a function of magnetic east-west distance. This random field attains its maximum fluctuation strength at the altitude of the F2 peak and at the center of the bubble ($\alpha = \alpha_0$), and it vanishes with angular distance from the bubble. We discuss the implications of this choice of bubble model in section 8.

[11] After performing the MPS calculation, we can transform spatial quantities (e.g., spectra) to temporal ones by assuming frozen-in flow and making the substitution $\Delta z \rightarrow V_s \Delta t$, where V_s is the velocity with which the propagation path scans through the irregularities. In summary, the parameters required to fully specify the scattering environment and execute the ROSS model are the standard deviation of density fluctuations $\sigma_{\Delta N/N}$, spectral slope ν, outer scale wave number k_0, vertical layer thickness L, horizontal bubble thickness L_H, horizontal bubble location z_0, distance between the bubble and the observation plane d_s, scan velocity V_s, peak density $NmF2$, peak height $hmF2$, and scale height H. We shall estimate these parameters using observations made by CORISS, ATLAIR, and SCINDA as described in sections 4–6. The only parameter we are not able to estimate from these observations is the outer scale wave number. Here we use $k_0 = 2\pi/L_0$ with $L_0 = 10$ km, which has been observed in other experiments [e.g., *Basu et al.*, 1983]. This value for L_0 is significantly larger than the Fresnel scale for any of the propagation geometries and frequencies considered here.

4. Observations From the CORISS Instrument Onboard C/NOFS

[12] The C/NOFS Occultation Receiver for Ionospheric Sensing and Specification (CORISS) instrument is a GPS dual-frequency receiver on board the C/NOFS satellite which measures line-of-sight TEC and GPS scintillations [*de La Beaujardière et al.*, 2004]. For this study we selected a radio occultation between GPS satellite PRN16 and the C/NOFS satellite that occurred on 21 April 2009 from 10:08:44 to 10:12:57 UT. The CORISS instrument collected 50 Hz samples of the signal-to-noise ratio (SNR) during this encounter. This particular occultation was selected based on

the following criteria: (1) scintillation of the GPS signal was observed, (2) the east-west occultation lines of sight (LOS) were approximately perpendicular to the magnetic field lines, (3) the occultation took place nearly in the plane of orbital motion, and (4) the occultation occurred near the ALTAIR radar and SCINDA VHF and GPS ground-based scintillation receivers. We use these auxiliary instruments (ALTAIR and SCINDA) to provide the geophysical parameters required by the density model. A geographic map showing the occultation geometry and the locations of the auxiliary instruments is given in Figure 2.

[13] Figure 3 shows the SNR observed by CORISS during this occultation starting at 10:08:44 UT and lasting roughly 4 min. From these observations we selected a 54 s interval between 10:09:11 UT and 10:10:05 UT (shown delimited by dotted lines in Figure 3) during which the statistics of the SNR fluctuations are approximately stationary. The power spectral density (PSD) of signal intensity fluctuations during this interval is shown in Figure 4. We used the maximum entropy method [*Fougere*, 1985] to compute this PSD and the other PSDs shown in this paper. The spectral slope of $p = 3.1$ was obtained by performing a least squares fit to the PSD in the logarithmic domain. The scintillation intensity index, S_4, is equal to the standard deviation of signal intensity normalized by the mean. During this time interval $S_4 = 0.25$, which implies the scatter is weak, and therefore the measured intensity and screen phase should have approximately the same spectral slope [*Yeh and Liu*, 1982]. Therefore, we will use this result to specify the spectral index $\nu = p/2 \approx 1.5$ for use in the MPS simulation. For reference purposes, during this time interval the altitude of the tangent point ranged from 280 to 340 km which, as we will demonstrate using measurements from ALTAIR (section 5), brackets the altitude of the F region density maximum.

[14] For weak scatter due to a thin layer of irregularities, the PSD of intensity fluctuations is simply related to the PSD of the total integrated phase advance due to propagation through the layer [*Yeh and Liu*, 1982]:

$$\Phi_I(K) = 4\sin^2\left(K^2\frac{\lambda d_s}{4\pi}\right)\Phi_\phi(K). \qquad (10)$$

In (10) K is the transverse spatial wave number, and d_s is the propagation distance past the scattering region to the receiver. The factor modulating the phase PSD, $\Phi_\phi(K)$, is referred to as the Fresnel filter function. Assuming that the medium does not evolve as the occultation line of sight scans through the medium with constant velocity, V_s, relative to the drifting plasma irregularities (frozen-flow hypothesis), we can infer the frequency power spectrum from the spatial power spectrum by substituting $K = 2\pi f/V_s$ in (10). For the case of a LEO satellite such as C/NOFS, the plasma velocity can be neglected in comparison with the component due to satellite motion. While *Yeh and Liu* [1982] derived (10) for the case of vertical propagation through a horizontal slab of plasma irregularities, here we apply it to the case of horizontal propagation through a plasma bubble. The Fresnel filter function in (10) has a maximum at the break frequency $f_b = V_s/(2\lambda d_s)^{1/2}$, and a sequence of local minima at the frequencies $f_n = V_s(n/\lambda d_s)^{1/2}$, where $n = 1, 2, \ldots$. Referring to Figure 4, we infer the break frequency for the CORISS occultation scintillation to
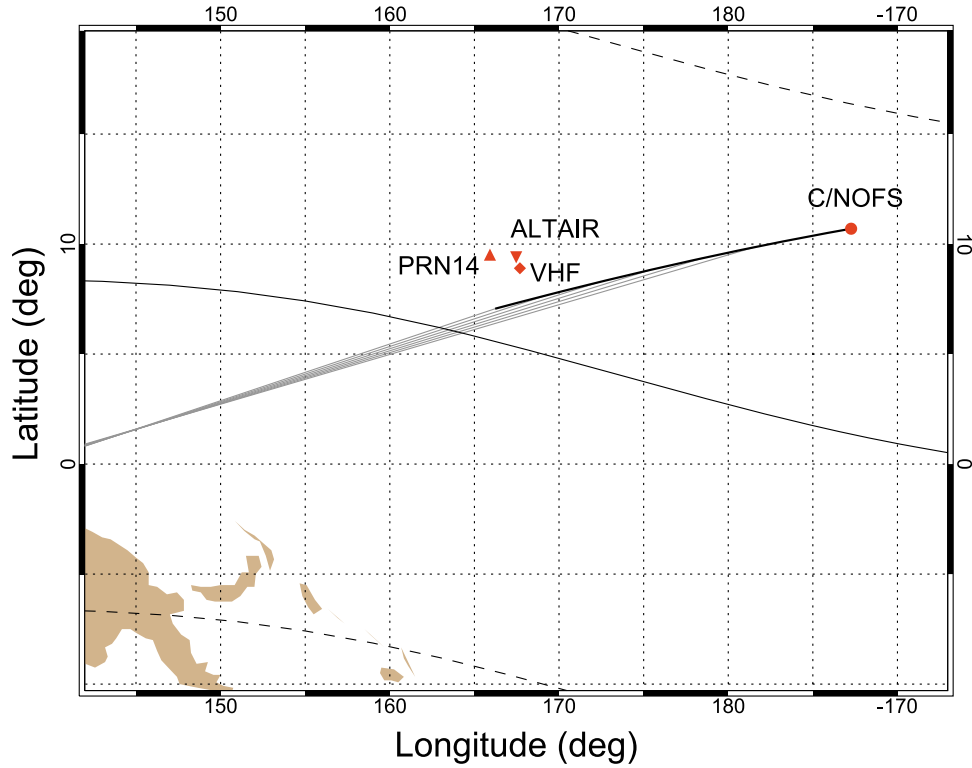
Figure 2. Geographic distribution of the data sources used to simulate the radio occultation between GPS PRN16 and the C/NOFS satellite on 21 April 2009 from 10:08:44 to 10:12:57 UT. The orbital track of the C/NOFS satellite during the occultation is shown as a thick solid line, while the circle shows its location at 10:12:57 UT. Grey lines from the C/NOFS satellite indicate the portion of the occultation lines of sight which lie between 250 and 400 km in altitude. Also shown are the locations of ALTAIR and the ionospheric penetration points for the VHF link to a geostationary satellite and for the ground-based GPS link to PRN14 at 10:43:14 UT. The curved solid line shows the geomagnetic dip equator, and the curved dashed lines show plus and minus 15° latitude from the dip equator.

be f_b = 1.39 Hz. Since the break frequency and Fresnel minima are related, the latter (when they are evident) can help to identify the former more precisely in intensity spectra [*Bhattacharyya et al.*, 1992]. The frequency spacing between the local minima in the intensity PSD shown in Figure 4

suggests that these are indeed Fresnel minima and we have used their locations as a guide to estimate the break frequency. The weak scatter result in equation (11) suggests a technique to infer the mean distance from the C/NOFS
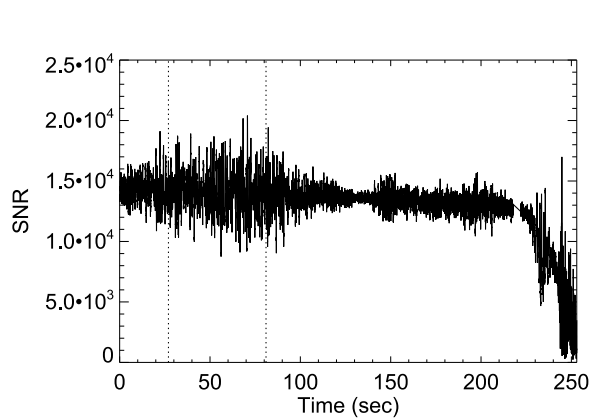

Figure 3. Signal-to-noise ratio observed by CORISS during an occultation with GPS PRN16 starting at 10:08:44 UT on 21 April 2009. Data during the 54 s interval between 10:09:11 and 10:10:05 UT (demarked by dotted lines) were selected for the PSD analysis shown in Figure 4.
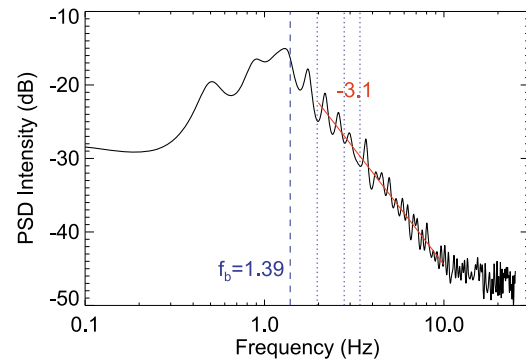

Figure 4. Power spectral density of the normalized intensity fluctuations shown in Figure 3 during the time window 10:09:11–10:10:05 UT. The dashed and dotted lines, respectively, show the inferred spectral break scale at f_b = 1.39 Hz and the corresponding locations of the first three Fresnel minima according to weak scatter theory. The spectral slope of the PSD is 3.1.

satellite to the bubble from the intensity PSD if the scan velocity is known, since

$$d_s = \frac{1}{2\lambda} \left(\frac{V_s}{f_b} \right)^2 \qquad (11)$$

This technique has been used by other authors to estimate the scan velocity when the height of the scattering layer is known [*Bhattacharyya et al.*, 1992]. The principal difficulty with using (11) to locate the scattering region for occultation scintillation is that the scan velocity must be known, but this depends on where the LOS penetrates the scattering region, which is not known a priori. For the case of space-to-ground propagation, a fixed height for the scattering layer is typically assumed. For the case of occultation scintillation, the scattering region can lie anywhere along the propagation path, in general. However, at L band frequencies we expect the scattering to occur mainly at altitudes close to the F region peak (especially during solar minimum when the density is smallest) and this does restrict the possible location of the bubble considerably. One possible solution to this problem would be to evaluate the scan velocity at the tangent point and then use (11) to estimate the distance to the scattering region, with the understanding that this will lead to an incorrect result if the scattering region is not actually close to the tangent point. A second approach which does not require this assumption is as follows. Neglecting the plasma drift velocity, we can obtain an expression for the scan velocity at the scattering location in terms of the distance from the C/NOFS satellite to the bubble:

$$V_s = V_\perp^{C/NOFS} + \frac{d_s}{d} \left[V_\perp^{GPS} - V_\perp^{C/NOFS} \right], \qquad (12)$$

where the subscript perpendicular indicates the component of velocity perpendicular to the LOS and d is the distance between the C/NOFS and GPS satellites. In (12) we have assumed the scan velocity for this particular occultation can be reasonably approximated by the perpendicular velocity because (1) the LOS scans through equatorial irregularities in a direction perpendicular to the magnetic field so that the irregularities appear to be isotropic and (2) the occultation takes place in the plane of the plane of orbital motion. The LOS for this particular occultation at the location of the scattering region is within 2° of orbital plane of the C/NOFS satellite, within 2° of the horizontal, and approximately 70° from the local magnetic field direction. For the general case, an anisotropy correction would be needed to account for the rate at which the LOS scans across elliptical isocontours of phase correlation. Solving the two equations (11) and (12) for the scan velocity and the distance to the scattering region simultaneously gives V_s = 984 m s^{-1} and d_s = 1317 km. Using the geometry of the LOS at the midpoint of the 54 s interval demarked by dotted lines in Figure 3, the location of the mean scattering region is determined to be (6.27°N, 164.0°E) at 315 km altitude. This is slightly westward of the tangent point location at this time, which was (6.59°N, 165.4°E) at 312 km altitude. A potential problem with this approach for locating the scattering region, in general, is that small errors in the measurement of the break frequency can lead to large errors in the estimated distance to the scattering region due its quadratic dependence on the break frequency. This approach also assumes that the signal has propagated through a single bubble, which is not always the case. Nevertheless, we show in section 5 that this estimate for the scattering location is within the region where coherent echoes were observed by ALTAIR. We note that *Sokolovskiy et al.* [2002] have used the alternative technique of back propagation to infer the distance to the scattering region. While we considered this option, the phase information from CORISS (required to back propagate the wave) was not available at the time of this study.

[15] Next, we estimate the strength of turbulence associated with the plasma bubble from the CORISS scintillation observations. If we compute the S_4 index for the 54 s interval demarked by dotted lines in Figure 3 we obtain S_4 = 0.25. Given an estimate for the propagation distance past the bubble (1317 km), and if we assume normal propagation with respect to the bubble, we can use equation (A5) to infer that the horizontally integrated strength of turbulence at the 1 km scale, $C_k L_H$, is approximately 2.93×10^{34} m^{-6}.

5. Observations From the ALTAIR Radar

[16] ALTAIR is a high-resolution radar located on the island of Roi-Namur in Kwajalein Atoll (9.4°N, 167.5°E). It provides tracking precision metrics, radar cross section (RCS) signature, and range-Doppler imaging for deep-space operations, satellite observations, strategic reentry missions, and multiple-intercept engagement tracking. Situated at 4.3°N magnetic dip latitude, the radar is also well suited for investigations of incoherent and coherent backscatter from the equatorial ionosphere [e.g., *Caton et al.*, 2009; *Hysell et al.*, 2006; *Tsunoda et al.*, 1979]. The fully steerable parabolic dish antenna (46 m diameter) operates in dual-frequency mode transmitting signals at 158 MHz (VHF) and 422 MHz (UHF).

[17] An east-west scan of the ALTAIR UHF radar in the plane perpendicular to the magnetic field (at F region altitudes), starting less than 5 min after the CORISS occultation occurred, is shown in Figure 5. The received signal was decoded, noise corrected, range corrected, and scaled to electron density units using a colocated ionosonde for calibration. Strong coherent echoes (plotted using a different color scale when they exceed a certain threshold SNR) are evident to the west of the radar between the altitudes of 250 and 400 km at this time. These coherent echoes are caused by Bragg scatter from small-scale plasma irregularities with characteristic size one half the radar wavelength, which is 36 cm for ATLAIR's UHF radar. Both the ALTAIR and CORISS data shown in Figure 5 have been mapped along magnetic field lines onto the magnetic equatorial plane to facilitate the comparison between them. The track swept out by the tangent point of the CORISS occultation in the magnetic equatorial plane is seen to traverse the coherent echoes observed by ALTAIR. For reference, 1 Hz averages of the CORISS SNR (in arbitrary units) is shown as a function of tangent point altitude in Figure 5 (right). A comparison of Figures 5 (left) and 5 (right) shows that, in large part, CORISS observed signal fluctuations when the tangent point intersected the coherent echoes detected by ALTAIR. For weak scatter in a power law environment, the dominant contribution to scintillation originates from irregularties with characteristic size close to the Fresnel scale,
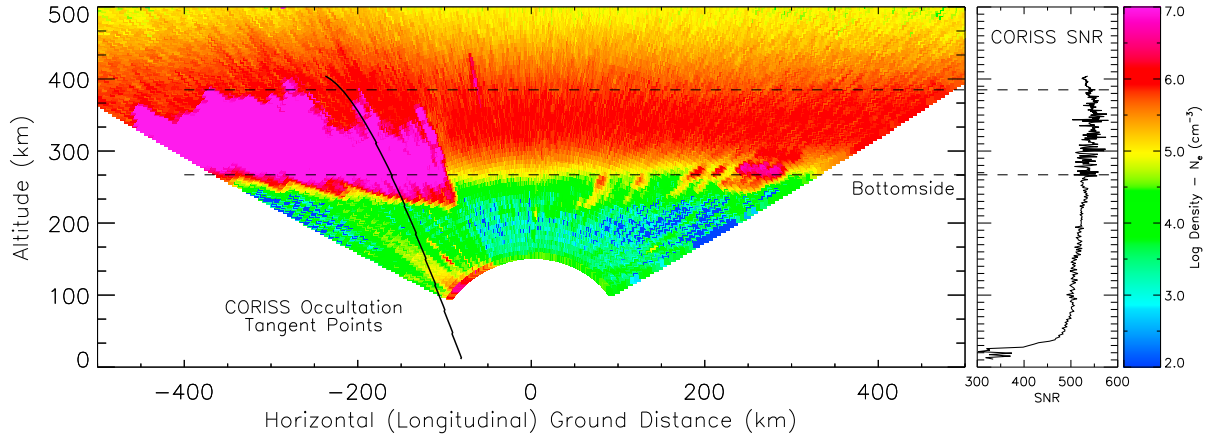
Figure 5. An east-west scan by the UHF ALTAIR radar in the plane perpendicular to the magnetic field (at F region altitudes). (left) The electron density calculated by the incoherent scatter technique and (right) the CORISS SNR (with arbitrary units) versus altitude of the tangent point. Both the ALTAIR and CORISS data have been mapped along magnetic field lines onto the magnetic equatorial plane to facilitate the comparison. The radar scan was performed using 1 s integration on 21 April 2009 between 10:13:13 UT and 10:21:06 UT, a few minutes after the CORISS occultation. The track of the tangent point for the CORISS occultation is plotted over the radar scan as a thick black curve. The regions of solid pink between approximately 250 and 400 km and located slightly west of the radar are coherent echoes from small-scale (36 cm) plasma irregularities. In this region, the radar cannot measure the electron density.

$(2\lambda d_s)^{1/2}$. In section 4, the distance from the receiver to the scattering region, d_s, was estimated to be 1317 km. Therefore, the CORISS observation is sensitive to scale sizes on the order of $(2\lambda_{GPS}\ d_s)^{1/2} \sim 708$ m. The fact that CORISS observed scintillation primarily at altitudes for which coherent echoes from ALTAIR were observed suggest that irregularities of order 708 m and 36 cm coexisted at this time, a scale ratio of nearly 2000. Note that CORISS detected ionospheric irregularities only within the F region, however, while the high sensitivity of ALTAIR also revealed structure at slightly lower altitudes. Also note that coherent echoes were detected slightly to the west of the CORISS tangent point track, which suggests the scattering region affecting the occultation is also located slightly westward of the tangent point. This is consistent with the location of the scattering region that we determined using spectral techniques in section 4. We will choose the location where the coordinates of ALTAIR map to the magnetic equatorial plane as the origin of our coordinate system for MPS simulation.

[18] The ROSS model scales the random density fluctuations used for the MPS simulation by a Chapman description of the background electron density profile in altitude according to equation (9). By integrating the radar returns shown in Figure 5 over time while excluding the coherent returns, a vertical electron density profile can be derived as shown in Figure 6. We fit a Chapman profile to the electron density measurements provided by ALTAIR with peak density $NmF2 = 8.81 \times 10^{11}$ m^{-3}, peak height $hmF2 = 288.5$ km, and scale height $H = 31$ km. Next, the ROSS model requires an estimate of scattering layer thickness which we obtain from the ALTAIR electron density profile as follows. It is generally assumed that most of the scattering of L band signals is concentrated within a thin layer surrounding the F2 peak [*Basu et al.*, 1983]. This is especially likely to be true during solar minimum conditions when electron density levels are at their lowest. Therefore,

we follow the approach used by *Wernik et al.* [2007] to estimate the scattering layer thickness as the distance between the heights at which the electron density falls to a fixed percentile of its peak value. Using a threshold of 75%, we infer the vertical thickness of the scattering layer to be approximately $L = 61$ km. We note that *Wernik et al.* [2007] use a threshold of 95%, which for our observations would imply a scattering layer thickness of only 15 km. An evaluation of the Fresnel filter function (not shown) corresponding to the Rytov solution for weak scatter through an extended layer [*Yeh and Liu*, 1982] suggests the intensity spectrum would have much deeper Fresnel minima than we
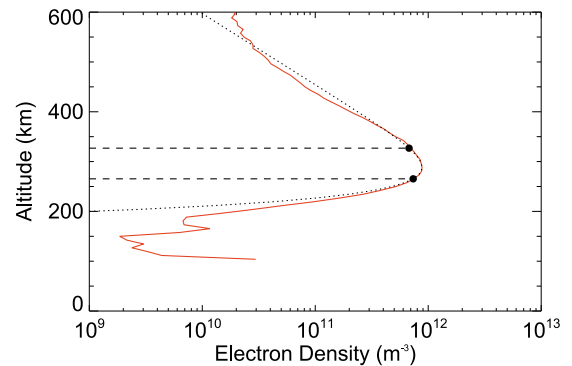

Figure 6. The vertical electron density profile obtained from ALTAIR by integrating the incoherent scatter observations from Figure 5 in time while excluding the coherent echoes. The dotted curve shows a Chapman profile defined by the peak density $NmF2 = 8.81 \times 10^{11}$ m^{-3}, peak height $hmF2 = 288.5$ km, and scale height $H = 31$ km. The dashed lines indicate the heights at which the electron density falls to 75% of its peak value. We use this to infer the vertical thickness of the scattering layer, which is $L = 61$ km.
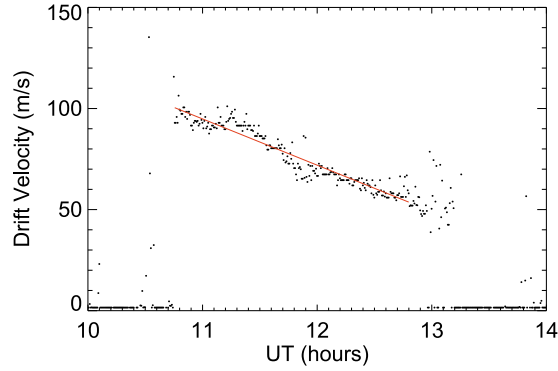
Figure 7. SCINDA VHF measurements of the zonal plasma drift velocity on 21 April 2009 obtained by cross-correlating scintillating signals from a geostationary satellite using a pair of magnetic east-west spaced VHF antennas. The solid line is a least squares fit to the drift velocity given by $V_d(t) = 346.5 - 0.006354(t)$, with t expressed in UT seconds since midnight and V_d in m s^{-1}.

observed if the layer were only 15 km thick. Therefore, we feel this thickness is too small and find that a threshold of 75% yields a result (61 km) which is more consistent with our observations.

6.   Observations From SCINDA

[19] The SCINDA network of ionospheric monitoring instruments is maintained by Air Force Research Laboratory and includes VHF and GPS scintillation receivers colocated with the ALTAIR radar on the island of Roi-Naumr [*Groves et al.*, 1997; *Caton et al.*, 2009]. The 244 MHz signal broadcasted by a geostationary communications satellite were monitored using spaced antennas and cross-correlated to obtain the zonal drift velocity on 21 April 2009 (Figure 7). These VHF receivers are separated by approximately 100 m in the magnetic east-west direction. A least squares fit to the drift velocity measurements gives $V_d(t) = 346.5 - 0.006354(t)$, with t expressed in UT seconds since midnight and V_d in m s^{-1}. The ionospheric penetration point (IPP) for the VHF link is located at (8.90°N, 167.7E°) which is approximately 426 km eastward of the mean scattering region detected by CORISS at (6.27°N, 164.0°E), as described in section 4. The zenith angle for this satellite link at the IPP is 13°. If the zonal drift velocity is approximately the same at these two locations simultaneously, we can compute the time at which the scattering region observed by CORISS should be detected later along the VHF link. The zonal drift velocity of the scattering region at 10:09:38 UT (the center of the time window demarked by dotted lines in Figure 3) is determined from the least squares fit to be $V_{di} = 114$ m s^{-1}. The velocity of the scattering region after it has drifted across the VHF link is given by $V_{df} = (V_{di}^2 + 2ad)^{1/2} = 87.2$ m s^{-1}, using $a = -0.006354$ m s^{-2} and $d = 4.26 \times 10^5$ m. This suggests the scattering region should drift across the VHF link in $2d/(V_{di} + V_{df}) = 4231$ s after the detection by CORISS, or at approximately 11:20:09 UT. The slant distance along the VHF link to the F region peak, using the estimate for $hmF2 = 288.5$ km provided by ALTAIR, is $d = 296$ km. The
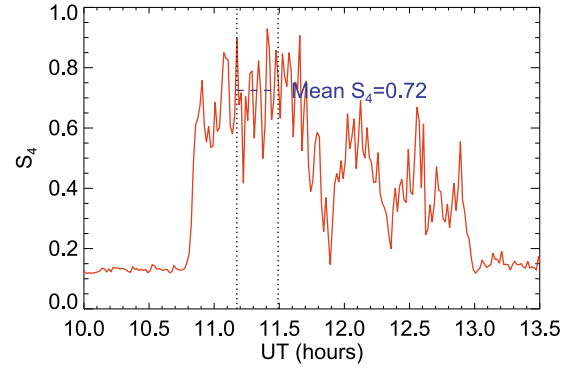

Figure 8. S_4 index measured by the VHF receiver at Kwajalein on 21 April 2009. The scattering region detected by CORISS should have arrived at the VHF link at approximately 11:20:09 UT. A 20 min window centered on this time is shown with dotted lines. The mean S_4 index during this time window was 0.72.

Fresnel scale for the VHF scintillation observations is then $(2\lambda_{VHF} d)^{1/2} \sim 842$ m.

[20] Figure 8 shows the S_4 index measured along the VHF satellite link on 21 April 2009. To account for some possible inaccuracy in the arrival time of the bubble, we selected a 20 min period centered on the time (11:20:09 UT) when the scattering region detected by CORISS should have drifted across the VHF link. The average S_4 value during this time window was 0.72. This value of S_4 implies the scatter at VHF is not weak, and therefore we cannot reliably employ the weak scatter relationships in Appendix A to estimate the strength of plasma turbulence from the VHF observations. As the scattering strength increases, irregularities with characteristic scale sizes other than the Fresnel scale size contribute significantly to the scattering. The Fresnel nulls disappear and the intensity spectrum has a tendency to broaden and steepen, making the break frequency more
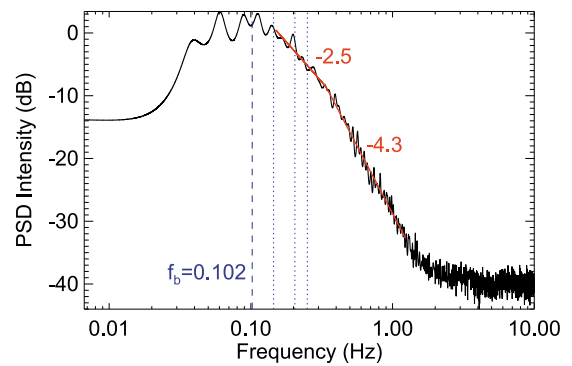

Figure 9. Power spectral density of normalized intensity fluctuations measured by the SCINDA VHF receiver (Figure 8) during the 20 min window centered at 11:20:19 UT. The Fresnel break scale (dashed line) was approximately $f_b = 0.102$ Hz. The frequencies corresponding to the first three Fresnel minima according to weak scatter theory are shown as dotted lines. A two-component spectrum with slopes 2.5 and 4.3 was observed, with a break scale near 0.3 Hz. For frequencies higher than approximately 2 Hz, the PSD is dominated by noise and should be ignored.
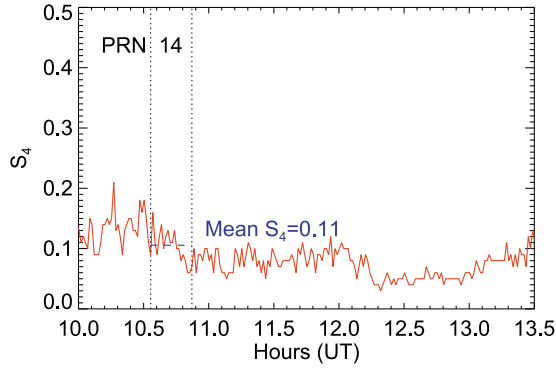
Figure 10. S_4 index for GPS PRN14 measured by the ground-based GPS receiver at Kwajalein on 21 April 2009. The scattering region detected by CORISS should have arrived at this link at approximately 10:43:14 UT. A 20 min window centered on this time is shown with dotted lines. The mean S_4 index during this time window was 0.11.

difficult to identify. Figure 9 shows the PSD of normalized intensity along the VHF link during this 20 min time window (surrounding 11:20:09 UT). This PSD shows some evidence of the spectral broadening and steepening characteristic of strong scatter. In this case no Fresnel rings are evident, but we can still identify the Fresnel break frequency as approximately $f_b = 0.102$ Hz. It is interesting to note that, even though the weak scatter relationship given in (11) is not strictly applicable, with $\lambda = 1.2$ m and $V_d = 87.2$ m s^{-1} this expression implies the slant distance to the scattering layer is 304 km. Accounting for the zenith angle at the IPP, the altitude of the scattering layer is determined to be 297 km, which is quite close to the altitude of the F region peak determined by ALTAIR (288.5 km).

[21] Colocated with the SCINDA VHF receiver at Roi-Naumr is an Ashtech Z-XII survey-grade GPS receiver which records 20 Hz samples of signal amplitude and phase.
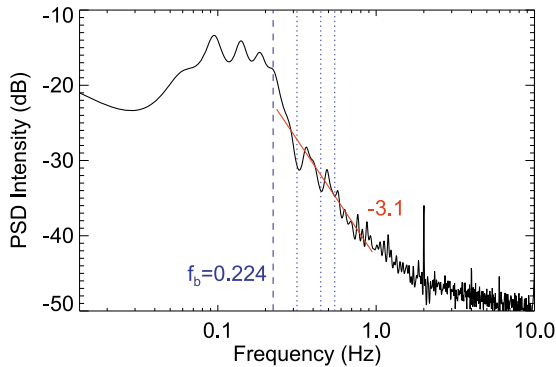
The S_4 index measured along the link to GPS PRN 14 on 21 April 2009 at the GPS L1 frequency (1575.42 MHz) is shown in Figure 10. Using the same approach as described above (except also accounting for the motion of the GPS satellite), we estimate that the scattering region observed by CORISS should have drifted into the line of sight to PRN14 at approximately 10:43:14 UT. We selected a 20 min window centered on this time, during which the mean value of S_4 was 0.11. Figure 11 shows the PSD of intensity during this 20 min window. The intensity spectrum for this space-to-ground GPS observation has a slope of 3.1. This is the same slope as the intensity spectrum for the space-to-space observation made by CORISS (Figure 4). Note that the Fresnel rings are more apparent in the GPS intensity PSD (Figure 11) than the VHF intensity PSD (Figure 9). This is not surprising since the scattering is significantly weaker along the GPS link than along the VHF link. The propagation (zenith) angle for the ground-based GPS link at the IPP was $\theta = 26°$ and the reduced vertical propagation range was $z_R = 302$ km. The Fresnel scale for the GPS scintillation observations is then $(2\lambda_{GPS} z_R \sec q)^{1/2} \sim 357$ m. If we use equation (A5) from Appendix A to estimate the turbulence strength parameter, we obtain $C_k L = 1.76 \times 10^{34}$ m^{-6}. If we again assume an outer scale of 10 km, equation (A6) implies that $\sigma_{\Delta N} = 1.50 \times 10^{11}$ m^{-3} and $\sigma_{\Delta N/N} = 17\%$.

[22] Before leaving this section, we use the observations from CORISS, ALTAIR, and the ground-based GPS receiver together to estimate the horizontal thickness of the plasma bubble. This is used to construct the bubble used for the MPS simulation. As mentioned earlier, weak scatter theory and the CORISS measurements of S_4 give an estimate for the horizontally integrated strength of turbulence as $C_k L_H = 2.93 \times 10^{34}$ m^{-6}. The ground-based GPS measurements of S_4 along the link to PRN14 give an estimate for the vertically integrated strength of turbulence $C_k L = 1.76 \times 10^{34}$ m^{-6}. The electron density profiles provided by ALTAIR give an estimate of the vertical thickness of the scattering layer, $L = 61$ km. We estimate the horizontal width of the
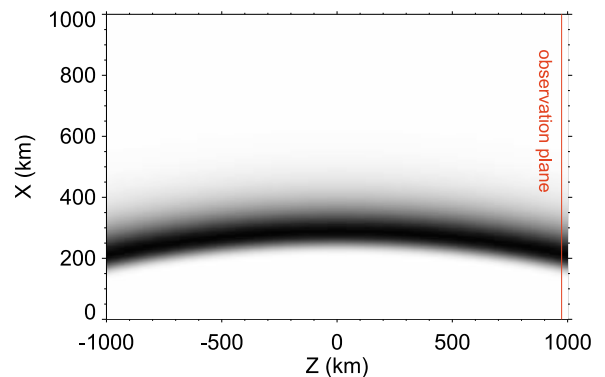

Figure 11. Power spectral density of the normalized intensity fluctuations for GPS PRN14 (Figure 10) during the 20 min window centered at 10:43:14 UT. For frequencies higher than approximately 2 Hz, the PSD is dominated by noise and should be ignored. The Fresnel break scale (dashed line) was approximately $f_b = 0.224$ Hz. The frequencies corresponding to the first three Fresnel minima according to weak scatter theory are shown as dotted lines.

Figure 12. Background electron density used for the multiple phase screen simulation. Darker shading signifies larger electron density. The origin of the coordinate system has been placed at the location where the ALTAIR radar maps to the magnetic equatorial plane. The observation plane indicates the plane where the field is sampled by CORISS.
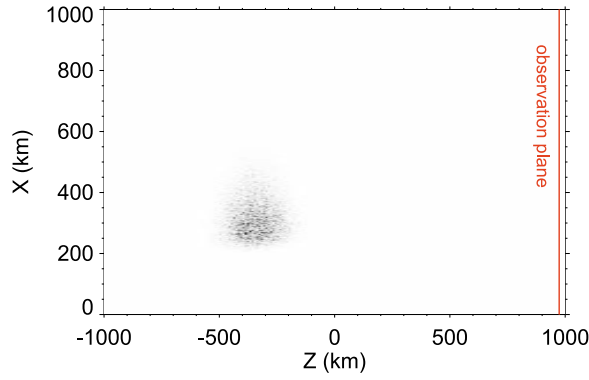
Figure 13. Absolute value of the random electron density fluctuations used in the multiple phase screen simulation.
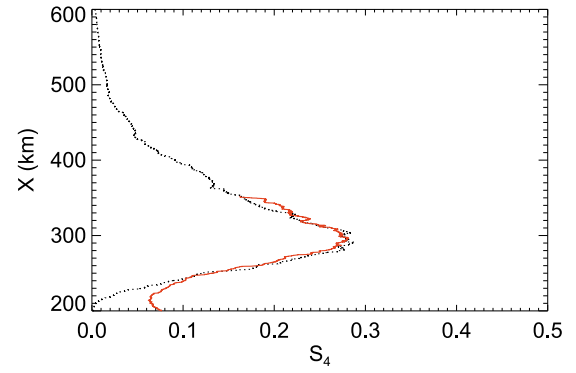
plasma bubble as the vertical thickness scaled by the ratio of horizontally to vertically integrated turbulence strength:

$$L_H = \left(\frac{C_k L_H}{C_k L} \right) L = 102 \text{ km} \qquad (13)$$

Thus, the horizontal width of the plasma bubble is 102 km. Note that this is the *effective* width of the bubble at L band, since it is computed from the horizontally integrated turbu-

Figure 15. Comparison between the MPS simulation (solid curve) and CORISS observations (dotted curve) of S_4 as a function of tangent point altitude.

lence strength, not necessarily the physical horizontal dimension of the bubble.

7. MPS Simulation Results

[23] In this section we show the results of our MPS simulation of scintillation along the occultation raypath observed by CORISS. The origin of the computational domain is placed at the location where the ALTAIR radar maps to the magnetic equatorial plane. A simulated bubble is intro-

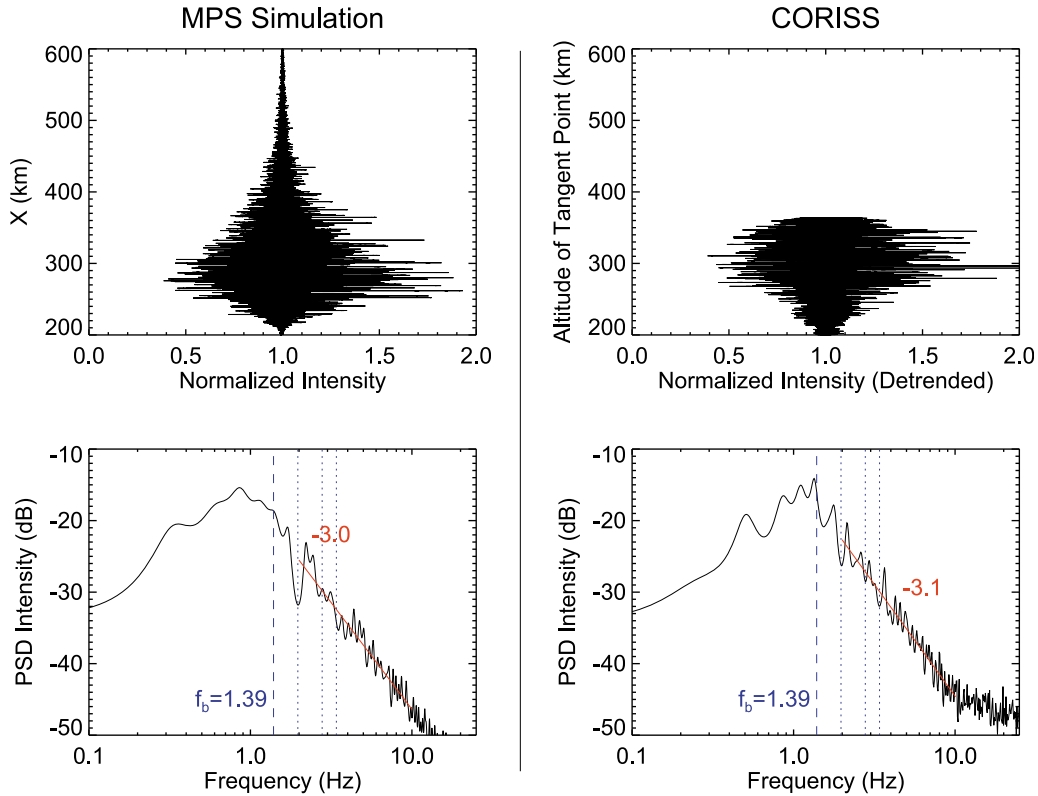**Figure 14.** Comparison between the MPS simulation and detrended CORISS observations. (top) The normalized intensity fluctuations versus altitude of the tangent point and (bottom) the PSD of normalized intensity fluctuations for tangent point altitudes between 280 and 340 km. The spectral break frequency and spectral index for the simulation are approximately the same as those determined from the CORISS observations.

Table 1. Parameters Used for the Multiple Phase Screen Simulation

Parameter	Value
$\sigma_{\Delta N/N}$	0.17
ν	1.5
k_0	$2\pi/10$ km
L	61 km
L_H	102 km
z_0	-342.8 km
d_s	1317 km
V_s	984 m s^{-1}
$NmF2$	8.81×10^{11} m^{-3}
$hmF2$	288.5 km
H	31 km

duced at $z_0 = -342.8$ km, and the observation plane sampled by C/NOFS is located 1317 km to the east of the bubble. The size of the computational grid is specified as 2000 km in the propagation (z) direction and 1000 km in the transverse direction (x). We use 2^{17} points along the transverse direction which gives a transverse resolution of 7.6 m, which is approximately 40 times the GPS L1 wavelength. Fewer points are required in the propagation direction since the field evolves much more slowly in this direction. We used 200 points in the propagation direction, giving a resolution of 10 km, which is equal to the outer scale of the random density fluctuations. The plane wave entering the computational domain at the western boundary penetrates 197 screens before reaching the observation plane. Prior to carrying out the occultation simulation, the algorithm was verified by propagating a plane wave vertically through the random density field, and comparing the resulting S_4 with that predicted by weak scatter theory. The ratio of simulated to predicted S_4 was 1.1 in this case.

[24] The geophysical parameters used in the MPS simulation are listed in Table 1. The background electron density constructed using these parameters is shown as a gray scale plot in Figure 12, where darker shading signifies larger electron density. The random realization of electron density fluctuations used in the simulation is shown in Figure 13, where darker shading implies larger $|\Delta N|$. The intensity fluctuations resulting from the MPS simulation are compared with detrended intensity fluctuations observed by CORISS in Figure 14. Both observations are shown as a function of tangent point altitude. The altitude profile of the simulated intensity fluctuations agrees quite well with the CORISS observations. Figure 14 also shows the PSD of intensity fluctuations between 280 and 340 km for both the MPS simulation and CORISS. The intensity PSD predicted by the MPS calculation has the same spectral slope and Fresnel break scale as the intensity PSD for the CORISS observations. Figure 15 shows the altitude profile of S_4 calculated from the MPS simulated intensity and the CORISS SNR observations using running statistics, evaluated with a centrally positioned 30 s window surrounding each data sample. The ratio of MPS predicted S_4 to CORISS observed S_4 throughout the altitude range 240–350 km ranged from 0.86 to 1.14, indicating a fairly high level of simulation accuracy. This altitude range approximately brackets the ionospheric scattering layer as we inferred it from ALTAIR. The small discrepancy below 240 km could possibly be

caused by the CORISS instrument sensing low level scintillations due to other plasma bubbles more distant from the tangent point, which we did not account for in our model. The MPS simulation is able to predict the S_4 for altitudes higher than those for which CORISS collected high rate observations. We note that the Planar Langmuir Probe (PLP) onboard the C/NOFS satellite [*de La Beaujardière et al.*, 2004] detected no evidence of in situ density fluctuations when the satellite flew over the region at this time because the satellite altitude (403 km) was slightly higher than the bubble.

8. Discussion

[25] The results presented in this paper suggest that scintillation along radio occultation raypaths can be modeled effectively by the multiple phase screen technique given an adequate specification of the ionospheric medium. The ROSS model reproduces the weak scatter observations considered here but is not limited to weak scatter or a thin homogeneous scattering layer. After the simulation, the complex scattered signal is available for analysis. This is an advantage over analytical approaches to the problem (such as those described in Appendix A) which provide only the signal moments. The excellent agreement between the vertical profiles of S_4 from the MPS simulation and from CORISS suggest that scaling the electron density fluctuations by the background electron density (i.e., assuming that $\Delta N/N$ is independent of altitude) was appropriate and that the scattering of the signal occurred primarily near the F region peak. Recent ALTAIR observations made by the authors suggest this is typical of recent solar minimum conditions when bubbles seldom break through into the topside ionosphere at Kwajalein. Despite these promising results, there are a few obvious questions and limitations of our approach, which we discuss in this section.

[26] The first limitation of our approach concerns our choice of density model. The equatorial plasma bubbles that we propagate through using the MPS technique are modeled as homogeneous density fluctuations modulated by a Chapman altitude profile and a Gaussian window in the magnetic east-west direction. In situ rocket and satellite experiments suggest that actual equatorial plasma bubbles consist of coherent structure imposed by the underlying plasma instability that created them [*Hysell*, 2000]. Using high resolution in situ plasma density measurements from the retarding potential analyzer (RPA) on the AE-E satellite and ground-based VHF and GPS scintillation receivers, *Basu et al.* [1983] determined that plasma bubbles are depletions in the otherwise relatively smooth ambient density. They also determined the strongest GPS scintillations occur in the high gradient regions associated with the eastern and western walls of the bubble. This scenario is not consistent with the distribution of density fluctuations in our simple bubble model, which are not embedded within a depletion in the background density, and where the fluctuation intensity is largest at the center of the bubble. More sophisticated plasma bubble models have been used in other radio propagation studies in which the variance of density fluctuations attains its peak value near the walls of the depletion [*Zernov et al.*, 2009]. Detailed propagation simulations, however, suggest that it is the total integrated phase variance which most strongly

affects propagation through an extended random medium, more so than the exact distribution of irregularities along the propagation path [*Kumagai*, 1987; *Booker et al.*, 1985]. For this reason, we spend considerable attention in this paper correctly specifying the total integrated phase variance (which is proportional to the density variance). Moreover, experimental studies have shown that while scintillation is caused by the bubble, its magnitude is determined by the magnitude of the background electron density that the bubble intersects [*Whalen*, 2009]. For this reason, we specify the background electron density carefully in the simulation using profiles derived from the ALTAIR incoherent scatter radar (section 5). *Rino and Carrano* [2011] address the problem of space-to-ground propagation through a more realistic plasma bubble.

[27] The simulation results from the ROSS algorithm are very sensitive to level of $\Delta N/N$ fluctuations present. Therefore, we should note that the outer scale (10 km) used to infer the RMS $\Delta N/N$ from the observations (and also to construct realizations of random density fluctuations) was not actually measured in our experiments. Nevertheless, so long as the same value is used when comparing horizontal and vertical propagation geometries, its influence on the simulation should not be important so long as L_0 is sufficiently larger than the Fresnel scale associated with the scattering. Here we have used space-to-ground scintillation observations to calibrate our space-to-space (occultation) scintillation simulations with the expectation that the dependence on outer scale will cancel. Also, we employed the weak scatter theory to infer the level of $\Delta N/N$ fluctuations from the signal fluctuations we observed. This weak scatter assumption is appropriate for the level of scatter we observed during these experiments. If the observed scatter were strong, it would be more difficult to accurately specify this fluctuation level for the MPS simulation. The MPS algorithm itself, however, is not limited to weak scatter scenarios.

[28] A second limitation of our approach concerns the restriction of the problem to occultations where the propagation is perpendicular to *B*, and that the occultation takes place in the plane of orbital motion. We assume the irregularities to be infinitely extended along the magnetic field direction so that a sequence of one-dimensional phase screens suffice to model propagation perpendicular to the magnetic field. This assumption is reasonable for both space-to-ground [e.g., *Knepp*, 1983] and also space-to-space propagation problems in the equatorial ionosphere where the magnetic field lines are approximately horizontal. Regarding our assumption that the irregularities are isotropic in the plane perpendicular to *B*, *Basu et al.* [1983] noted the similarity between spectra obtained from horizontal satellite observations and vertical rocket observations at Kwajalein, both in the plane perpendicular to *B*. We observed the same spectral slope for the CORISS observations along the space-to-space propagation geometry as with the space-to-ground GPS measurements. Restricting the problem to the plane perpendicular to *B*, however, limits the applicability of our model to east-west occultation geometries. While this condition is met for specific radio occultation observations made by the C/NOFS satellite, it is unlikely to be met for occultation observations made by satellites with high orbital inclinations such as COSMIC, CHAMP, SAC-C, or PICOSat4.

[29] A complete simulation methodology for radio occultation propagation must account for the time-dependent geometry of the ionospheric penetration point along the line of sight between the transmitting and receiving antennas, relative to the plasma drift, while accounting for the elongation of the irregularities along the magnetic field. Earlier works have shown that the angle of propagation with respect to the magnetic field has a pronounced effect on the intensity of radio occultation scintillation [*Anderson and Straus*, 2005]. These geometrical issues must also be addressed in order to compare the temporal spectra observed in experiments with the spatial spectra produced by our simulations.

9. Conclusions

[30] Instruments onboard low Earth orbiting satellites routinely collect radio occultation observations using signals transmitted by the GPS constellation of satellites, providing a rich source of information about the global occurrence morphology of ionospheric scintillation. Radio occultation monitoring of scintillation has the advantage that it can be performed on a global basis more easily than using ground-based monitoring techniques. Despite the advantage of global coverage, however, the long propagation path of a radio occultation through the ionosphere makes it difficult to determine the geographic location and spatial extent of the plasma irregularities responsible for the scintillation. Moreover, it is not obvious from the radio occultation signal itself what specific configuration of the plasma has modulated the signal. To address these concerns, we have developed the Radio Occultation Scintillation Simulator (ROSS) which uses the multiple phase screen (MPS) method to simulate the forward scatter of radio occultation signals by irregularities in the equatorial ionosphere.

[31] We use a simple approach to simulate propagation through equatorial plasma bubbles, which are modeled as homogeneous random fluctuations with an outer scale and single slope power law, modulated by a Chapman altitude profile and a Gaussian window in the magnetic east-west direction. The spatial distribution of the fluctuation strength is assumed to scale with the background electron density. A plane wave is propagated through the inhomogeneous random density field along the radio occultation path using the multiple phase screen method to obtain the signal at the receiver. After the simulation, the complex scattered signal is available for analysis. This is an advantage over analytical approaches to the problem, which generally provide only the moments.

[32] We adjust the parameters of the density model using vertical density profiles derived from incoherent scans made by the ALTAIR radar (9.4°N, 167.5°E, 4.3° north dip), and space-to-ground observations of scintillation using VHF and GPS receivers that are colocated with the radar. The east-west scan of ALTAIR perpendicular to the magnetic field revealed coherent echoes to the west of the radar at altitudes confined to a relatively narrow F region (the scale height was 31 km). The scintillation observations made by CORISS and the ground-based GPS receiver were characterized by the same spectral index of $p = 3.1$. A spectral analysis technique was used to simultaneously identify the scattering region along the occultation line of sight and estimate the scan velocity through the irregularities. The location of the scattering region inferred from the CORISS scintillation observations is in qualitative agreement with

the locations where ALTAIR observed coherent echoes. This suggests the coexistence of irregularity sizes on the order of 708 m (the Fresnel zone radius for the CORISS observations) and 36 cm (the Bragg scale for the ALTAIR scans). VHF scintillation observations were used to infer the zonal plasma drift (54–100 m s^{-1}) and also altitude of the scattering layer (297 km) which is found to be consistent with the F2 region peak observed by ALTAIR (288 km). Space-to-ground GPS scintillation observations provided an estimate for the level of RMS ΔN/N fluctuations (17%). A comparison of space-to-space and space-to-ground scintillation observations enabled us to estimate the horizontal extent of the plasma bubble to be 102 km.

[33] We compare the simulated scintillating signal to observations of scintillation from CORISS during a radio occultation occurring near ALTAIR. The ratio of MPS predicted S_4 to CORISS observed S_4 throughout the F region altitudes of 240–350 km ranged between 0.86 and 1.14. These results suggest that scintillation along radio occultation raypaths can be modeled effectively by the multiple phase screen technique given an adequate specification of the ionospheric medium. This good agreement for the vertical profile of S_4 suggests that scaling the density fluctuations with the background density (which assumes the RMS ΔN/N is independent of altitude) was appropriate, and that the scattering of the signal occurred primarily near the F region peak.

[34] Future development of the ROSS algorithm will involve the use of a more realistic bubble model in which the random fluctuations are embedded in a density depletion with increased strength near the walls of the bubble, as has been observed in some scintillation experiments. Part of this effort is reflected in the paper by *Rino and Carrano* [2011], in which a plasma bubble derived from an electrodynamics model is used to explore the effects of deterministic structure on space-to-ground radio propagation. How small-scale structure (turbulence) within a plasma bubble is related to the surrounding large-scale density depletion in which it is embedded, is still a largely open physics question that should be addressed in order to refine propagation models and facilitate the interpretation of occultation scintillation measurements. A generalization of the ROSS model to accommodate arbitrary propagation geometries with respect to magnetic field will likely be necessary to simulate occultation observations made by satellites with higher orbital inclinations than C/NOFS.

Appendix A

[35] *Rino and Fremouw* [1977] and *Rino* [1979] showed that for propagation through a thin layer of ionospheric irregularities in the Born approximation (single scatter), the S_4 index can be expressed as

$$S_4^2 = r_e^2 \lambda^2 C_s L \sec\theta \left(\frac{\lambda z_R \sec\theta}{4\pi} \right)^{\nu-1/2} \frac{\Gamma[(2.5-\nu)/2]}{2\sqrt{\pi}\Gamma[(\nu+0.5)/2](\nu-0.5)} F \tag{A1}$$

where

r_e classical electron radius (2.818×10^{-15} m);
λ wavelength;
C_s strength of the 3-D spatial spectrum of turbulence at a wave number of 1 rad m^{-1};

z_R reduced vertical propagation range;
L thickness of the scattering layer;
θ zenith angle of propagation;
Γ Euler's gamma function;
F a combined geometry and propagation factor.

[36] The spectral slope, ν, is defined such that $p = 2\nu$ is the phase spectral index and $p^{(3)} = 2\nu + 1$ is the spectral slope of three-dimensional in situ density fluctuations. The reduced vertical propagation range corrects for the spherical curvature of the wavefronts and is given by $z_R = z_1 z_2/(z_1 + z_2)$, where z_1 and z_2 are the vertical distances from the receiver and transmitter to the phase screen, respectively. For highly elongated irregularities traversed in a direction well away from along their principal axis, the factor F is given by

$$F = \frac{\Gamma(\nu)}{\sqrt{\pi}(\nu + 1/2)}. \tag{A2}$$

[37] The strength of turbulence is related to the standard deviation of electron density fluctuations, σ_N, as

$$C_s = 8\pi^{3/2}\sigma_N^2 k_0^{2\nu-2} \frac{\Gamma(\nu + 1/2)}{\Gamma(\nu - 1)}, \tag{A3}$$

where $k_0 = 2\pi/L_0$ is the outer scale wave number and L_0 is the outer scale. It is convenient to introduce $C_k L$, the vertically integrated strength of turbulence at the 1 km length scale, which is related to C_s according to

$$C_k L = \left(\frac{1000}{2\pi} \right)^{2\nu+1} C_s L. \tag{A4}$$

While these results were derived for the case of space to ground propagation, we will also apply them to the occultation geometry, and we write $C_k L_H$ to indicate the horizontally integrated strength of turbulence in direct analogy to $C_k L$.

[38] When the phase spectral index is 3 (i.e., $\nu = 1.5$) the expressions (A1)–(A4) simplify considerably so that

$$C_k L = \frac{S_4^2}{\pi^3 r_e^2 \lambda^2 \sec\theta} \left(\frac{1000^4}{\lambda z_R \sec\theta} \right), \tag{A5}$$

gives the strength of turbulence in terms of measurements of S_4. The layer thickness need not be known in order to characterize the strength of turbulence in this formulation, which is an advantage. In this case, the variance of electron density fluctuations can be estimated from $C_k L$ as

$$\sigma_{\Delta N}^2 = \frac{1}{8\pi L k_0} \left(\frac{2\pi}{1000} \right)^4 C_k L, \tag{A6}$$

but note that both L and k_0 are required and typically known only approximately. Once $\sigma_{\Delta N}$ is has been determined, $\sigma_{\Delta N/N}$ is calculated by dividing by the peak background electron density, $NmF2$.

References

Aarons, J. (1982), Global morphology of ionospheric scintillations, *Proc. IEEE*, *70*(4), 360–378, doi:10.1109/PROC.1982.12314.

Anderson, P. C., and P. R. Straus (2005), Magnetic field orientation control of GPS occultation observations of equatorial scintillation, *Geophys. Res. Lett.*, *32*, L21107, doi:10.1029/2005GL023781.

Basu, S., Su. Basu, J. P. McClure, W. B. Hanson, and H. E. Whitney (1983), High resolution topside in situ data of electron densities and VHF/GHz scintillations in the equatorial region, *J. Geophys. Res.*, *88*, 403–415, doi:10.1029/JA088iA01p00403.

Basu, S., K. M. Groves, Su. Basu, and P. J. Sultan (2002), Specification and forecasting of scintillations in communication/navigation links: Current status and future plans, *J. Atmos. Sol. Terr. Phys.*, *64*, 1745–1754, doi:10.1016/S1364-6826(02)00124-4.

Béniguel, Y. (2002), Global Ionospheric Propagation Model (GIM): A propagation model for scintillations of transmitted signals, *Radio Sci.*, *37*(3), 1032, doi:10.1029/2000RS002393.

Bhattacharyya, A., K. C. Yeh, and S. J. Franke (1992), Deducing turbulence parameters from transionospheric scintillation measurements, *Space Sci. Rev.*, *61*, 335–386, doi:10.1007/BF00222311.

Booker, H. G., J. A. Ratcliffe, and D. H. Shinn (1950), Diffraction from an irregular screen with applications to ionospheric problems, *Philos. Trans. R. Soc. London A*, *242*, 579–607, doi:10.1098/rsta.1950.0011.

Booker, H. G., J. A. Ferguson, and H. O. Vats (1985), Comparison between the extended-medium and the phase-screen scintillation theories, *J. Atmos. Terr. Phys.*, *47*, 381–399, doi:10.1016/0021-9169(85)90018-2.

Carrano, C. S., and K. M. Groves (2006), The GPS segment of the AFRL-SCINDA global network and the challenges of real-time TEC estimation in the equatorial ionosphere, paper presented at the 2006 National Technical Meeting, Inst. of Navig., Monterey, Calif.

Caton, R. G., C. S. Carrano, C. M. Alcala, K. M. Groves, T. Beach, and D. Sponseller (2009), Simulating the effects of scintillation on transionospheric signals with a two-way phase screen constructed from ALTAIR phase-derived TEC, *Radio Sci.*, *44*, RS0A12, doi:10.1029/2008RS004047.

Costa, E., and S. Basu (2002), A radio wave scattering algorithm and irregularity model for scintillation predictions, *Radio Sci.*, *37*(3), 1046, doi:10.1029/2001RS002498.

de La Beaujardière, O., et al. (2004), C/NOFS: A mission to forecast scintillations, *J. Atmos. Sol. Terr. Phys.*, *66*, 1573–1591, doi:10.1016/j.jastp.2004.07.030.

Fougere, P. F. (1985), On the accuracy of spectrum analysis of red noise processes using maximum entropy and periodogram methods: Simulation studies and application to geophysical data, *J. Geophys. Res.*, *90*, 4355–4366, doi:10.1029/JA090iA05p04355.

Goodman, J. W. (2005), *Introduction to Fourier Optics*, 3rd ed., Roberts, Englewood, Colo.

Grimault, C. (1998), A multiple phase screen technique for electromagnetic wave propagation through random ionospheric irregularities, *Radio Sci.*, *33*, 595–605, doi:10.1029/97RS03552.

Groves, K., et al. (1997), Equatorial scintillation and systems support, *Radio Sci.*, *32*, 2047–2064, doi:10.1029/97RS00836.

Hysell, D. L. (2000), An overview and synthesis of plasma irregularities in equatorial spread F, *J. Atmos. Sol. Terr. Phys.*, *62*, 1037–1056, doi:10.1016/S1364-6826(00)00095-X.

Hysell, D. L., M. F. Larsen, C. M. Swenson, A. Barjatya, T. F. Wheeler, T. W. Bullett, M. F. Sarango, R. F. Woodman, J. L. Chau, and D. Sponseller (2006), Rocket and radar investigation of background electrodynamics and bottom-type scattering layers at the onset of equatorial spread F, *Ann. Geophys.*, *24*, 1387–1400, doi:10.5194/angeo-24-1387-2006.

Karayel, E. T., and D. P. Hinson (1997), Sub-Fresnel-scale vertical resolution in atmospheric profiles from radio occultations, *Radio Sci.*, *32*, 411–423, doi:10.1029/96RS03212.

Knepp, D. L. (1983), Multiple phase-screen calculation of the temporal behavior of stochastic waves, *Proc. IEEE*, *71*(6), 722–737, doi:10.1109/PROC.1983.12660.

Kumagai, H. (1987), Spatial correlations in intense ionospheric scintillations: Comparison between numerical computation and observation, *Radio Sci.*, *22*, 439–448, doi:10.1029/RS022i003p00439.

Rino, C. L. (1979), A power law phase screen model for ionospheric scintillation: 1. Weak scatter, *Radio Sci.*, *14*, 1135–1145, doi:10.1029/RS014i006p01135.

Rino, C. L. (2011), *The Theory of Scintillation With Applications in Remote Sensing*, John Wiley, Hoboken, N. J.

Rino, C. L., and C. S. Carrano (2011), The application of numerical simulations in Beacon scintillation analysis and modeling, *Radio Sci.*, *46*, RS0D02, doi:10.1029/2010RS004563.

Rino, C. L., and E. J. Fremouw (1977), The angle dependence of singly scattered wavefields, *J. Atmos. Terr. Phys.*, *39*, 859–868, doi:10.1016/0021-9169(77)90166-0.

Ruggiero, F. H., K. M. Groves, M. J. Starks, and T. L. Beach (2009), Comparisons of space-based GPS occultation ionospheric scintillation measurements with ground-based VHF measurements, paper presented at the Sixth Symposium on Space Weather, Am. Meteorol. Soc., New Orleans, La., Jan.

Sokolovskiy, S. V. (2001), Modeling and inverting radio occultation signals in the moist troposphere, *Radio Sci.*, *36*, 441–458, doi:10.1029/1999RS002273.

Sokolovskiy, S., W. Schreiner, C. Rocken, and D. Hunt (2002), Detection of high-altitude ionospheric irregularities with GPS/MET, *Geophys. Res. Lett.*, *29*(3), 1033, doi:10.1029/2001GL013398.

Straus, P. R., P. C. Anderson, and J. E. Danaher (2003), GPS occultation sensor observations of ionospheric scintillation, *Geophys. Res. Lett.*, *30*(8), 1436, doi:10.1029/2002GL016503.

Tsunoda, R. T., M. J. Baron, J. Owen, and D. M. Towle (1979), ALTAIR: An incoherent scatter radar for equatorial spread F studies, *Radio Sci.*, *14*, 1111–1119, doi:10.1029/RS014i006p01111.

Wernik, A. W., L. Alfonsi, and M. Materassi (2007), Scintillation modeling using in situ data, *Radio Sci.*, *42*, RS1002, doi:10.1029/2006RS003512.

Whalen, J. A. (2009), The linear dependence of GHz scintillation on electron density observed in the equatorial anomaly, *Ann. Geophys.*, *27*, 1755–1761, doi:10.5194/angeo-27-1755-2009.

Yeh, K. C., and C.-H. Liu (1982), Radio wave scintillations in the ionosphere, *Proc. IEEE*, *70*(4), 324–360, doi:10.1109/PROC.1982.12313.

Zernov, N. N., V. E. Gherm, and H. J. Strangeways (2009), On the effects of scintillation of low-altitude bubbles on transionospheric paths of propagation, *Radio Sci.*, *44*, RS0A14, doi:10.1029/2008RS004074.

C. S. Carrano, Institute for Scientific Research, Boston College, 140 Commonwealth Ave., Chestnut Hill, MA 02467-3862, USA. (charles.carrano@bc.edu)

R. G. Caton, Air Force Research Laboratory, Space Vehicles Directorate, Kirtland AFB, NM 87117, USA. (Ronald.Caton@kirtland.af.mil)

K. M. Groves, Air Force Research Laboratory, Space Vehicles Directorate, Hanscom AFB, MA 01731, USA. (keith.groves@hanscom.af.mil)

C. L. Rino, Rino Consulting, 471 Claremont Way, Menlo Park, CA 94025, USA. (crino@mindspring.com)

P. R. Straus, The Aerospace Corp., PO Box 92957, El Segundo, CA 90009, USA. (paul.r.straus@aero.org)